Lawrence Berkeley National Laboratory
LBL Publications

Title

Controlling phase separation in vanadium dioxide thin films via substrate engineering

Permalink
https://escholarship.org/uc/item/87k157h6

Journal
Physical Review B, 96(16)

ISSN
2469-9950

Authors
Corder, Stephanie N Gilbert
Jiang, Jianjuan
Chen, Xinzhong
et al.

Publication Date
2017-10-01

DOI
10.1103/physrevb.96.161110

Peer reviewed

eScholarship.org Powered by the California Digital Library
University of California

Controlling mesoscopic phase separation in highly oriented vanadium dioxide thin films via substrate engineering

S. N. Gilbert Corder[1,+], Jianjuan Jiang[2,+], Xinzhong Chen[1], Salinporn Kittiwatanakul[3], I-Cheng Tung[4], Yi Zhu[4], Jiawei Zhang[1], Hans A. Bechtel[5], Michael C. Martin[5], Jiwei Lu[3], Stuart A. Wolf[3,6], Haidan Wen[4,*] Tiger Hu Tao[2,7,*], Mengkun Liu[1,*]

1. Department of Physics, Stony Brook University, Stony Brook, New York 11794, USA
2. State Key Laboratory of Transducer Technology, Shanghai Institute of Microsystem and Information Technology, Chinese Academy of Sciences, Shanghai 200050, China
3. Department of Materials Science and Engineering, University of Virginia, Charlottesville, Virginia 22904, USA
4. Advanced Photon Source, Argonne National Laboratory, Argonne, Illinois 60439, USA
5. Advanced Light Source, Lawrence Berkeley National Laboratory, Berkeley, California 94720, USA
6. Department of Physics, University of Virginia, Charlottesville, Virginia 22904, USA
7. Department of Mechanical Engineering the University of Texas at Austin, Austin, TX 78712, USA

+ Contributed equally
* Corresponding authors

Understanding, designing, and manipulating phase transitions at microscopic length scales in a chemically homogeneous system is a central goal of strongly correlated electron material research. The strong electron-lattice interactions in correlated electron systems provide unique opportunities for altering the material properties with relative ease and flexibility. In this work, we use localized strain control via a focused-ion-beam-patterning of a substrate to demonstrate that one can selectively engineer the insulator-to-metal transition temperature, the fractional component of the insulating and metallic phases, and the degree of optical anisotropy down to ~100 nm length scales in VO_2 thin films. The effects of localized strain control on the strongly correlated system are directly visualized by state-of-the-art IR near-field imaging and spectroscopy techniques and X-ray micro-diffraction measurements.

Phase separation and coexistence are universal phenomena in strongly correlated electron materials (SCEM). The associated energy and length scales at which the phase inhomogeneities and separation occur are directly related to the microscopic electron and lattice structures. Several pathways exist for modifying the properties of SCEM and controlling the phase separation at relevant length scales. Such paths include local electric-field gating [1–5], ion

beam implantation [6], and light-induced phase transitions [7–9]. The electric-field-induced effects can alter the phase inhomogeneities in a quasi-controllable manner and ion implantation allows for spatially-selective phase engineering by introducing local defects and substitutions of atoms. While these methods have generated considerable interest for controlling SCEM, they have their own limitations: the high gate voltages often require the fabrication of nano-electrodes, making control of local fields across macroscopic length scales difficult. Ion implantation is costly and can induce local structural defects, which may add extrinsic factors to the phase transitions. Light-induced inhomogeneities are restricted to the diffraction-limited spot size and are often transient effects – the inhomogeneities disappear when the light is switched off. In contrast to previous methods which rely on directly altering the SCEM films, we demonstrate a different route for controlling phase inhomogeneities down to the nano-scale: interface engineering. As will be shown below, this new method possesses several unique advantages for modifying the local properties in SCEM including reduced chemical defects, ease of thin film growth, no post-fabrication processing, and direct control of the extent of the inhomogeneities.

This research is motivated by previous investigations of the phase separation of vanadium dioxide (VO_2) thin films at elevated temperatures [5,10–12]. IR near-field imaging studies revealed that the phase transition temperature and the microscopic phase separation patterns of VO_2 films vary considerably when grown on different substrates [10,13]. These distinct substrate and film thickness dependent mesoscopic patterns in highly oriented transition metal oxide thin films originate from the epitaxial strain due to lattice mismatch [10,14–16]. For example, in VO_2 films on a $(110)_R$ TiO_2 substrate with an in-plane rutile c_R axis, stripe-like unidirectional phase separations are evident [11]. These metallic stripes can extend throughout the entire sample for a typical sample size of around 5 × 5 mm. The width and periodicity of the stripes are typically sub-μm, depending on the sample thickness [11]. In VO_2 films on sapphire substrates (e.g. c-Al_2O_3), however, a randomized metallic nucleation takes place rather than pattern formation [17,18]. The substrate-dependent phase inhomogeneities for the different films is mainly the result of distinct elastic coupling and epitaxial strain between the VO_2 and the substrate lattice. The complex, self-organized elastic interactions at the interface lead to variations in transition temperature and electronic phase separation in the VO_2 films.

The epitaxial strain initiated local texture formation provides an opportunity for microscopic

engineering of functional SCEM materials at the nanoscale. By introducing microscopic roughness and exposing different facets of the substrates before depositing the films, one can effectively control the interfacial strain and thus the phase transition properties of the subsequent SCEM films. The engineered mixed electronic phases can be studied with nano-scale resolution using near-field imaging and spectroscopy. The crystal structure of the SCEM film can be further characterized with micro-x-ray diffraction (μ-XRD) to provide a direct characterization of the local lattice parameters and structural phase composition with sub-micron resolution.

Results

Sample Fabrication. We use focused ion beam (FIB) to create checkerboard patterns on $(110)_R$ TiO_2 substrates before VO_2 film deposition. Within the patterned region, part (50%) of the surface is masked, part (50%) is exposed to the beam as squares. The typical applied voltage for the ion beam lithography is ~30 keV, with the beam current ~24 pA (strata FIB 201, FEI Co., Ga ions). Patterns of different sizes (e.g., 200 nm, 500 nm, 1 μm, 5 μm) and different alignment angles (e.g., 0°， 30°, 45° with respect to the $(001)_R$ axis) are created on the same substrate. The entire fabrication procedure is schematically shown in Fig. 1 (a) and the actual patterns can be seen in the Supplemental Materials Fig. S1. The FIB etches the substrate surface to a depth of a few nm to a hundred nm. The high energy ions also modify the structure by exposing different crystal facets in the TiO_2 along their collision path. The size of the structurally modified region depends on the dosage of the incident ion beam and the degree of beam spot dispersion [19]. Based on our experimental parameters, the structurally modified region is estimated to have a spatial extent of about 200 nm in depth and also exist at the border of the masked/unmasked regions.

A VO_2 thin film is then grown on the patterned substrate using reactive bias target ion beam deposition at a substrate temperature of 400° C under 5.5 sccm Ar/O_2 80/20 mixture flow. The details on the growth technique can be found elsewhere [20,21]. The VO_2 film thickness is estimated to be 71 nm with <5 nm variation across the entire pattern. As a result of the FIB patterning, the VO_2 displays increased roughness in the checkerboard regions as compared to the single crystal thin film in the unpatterned areas (see the Supplemental Materials Fig. S2). The

disruption of the $(110)_R$ TiO_2 surface alters the orientation of the VO_2 in the patterned regions and is shown schematically as an interface cross section in Fig. 1 (b).

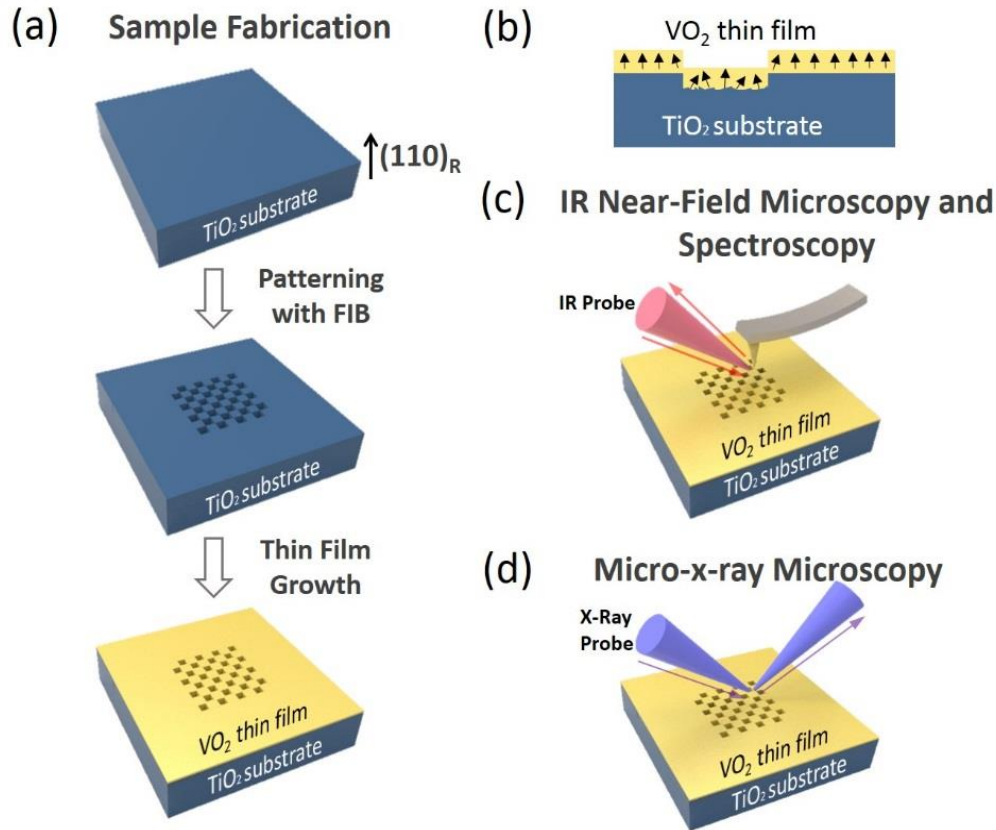

Figure 1 │Experimental Design. (a) The samples are fabricated by patterning TiO_2 $(110)_R$ substrates with a focused ion beam to produce a checkerboard pattern. After patterning, a VO_2 thin film (~71 nm) is grown over the substrate. The strain relief caused by the patterning of the substrate locally disrupts the VO_2 overgrowth, producing microscopic regions of different crystallinity. (b) Schematic cross section of the VO_2/TiO_2 interface showing the effects of etching and structural modification. The growth on the patterned regions produces a less coherent VO_2 film as different TiO_2 crystal facets are exposed by etching. (c) The local electronic phase transitions of the patterned samples are investigated with imaging and broadband spectroscopic s-SNOM with ~10 nm resolution. (d) The local crystallinity and structural phase transition of the VO_2 film are explored with micro-XRD with < 1 μm resolution.

Near-Field and μ-XRD Characterization at Room Temperature. In order to probe the electronic properties at the nano-scale, scattering scanning near-field optical microscopy (s-SNOM) is used to image the IR properties of the samples at single frequencies (10-11 μm) or collect spectra at specific locations with a broadband light source. The infrared near-field apparatus has ~10 nm spatial resolution (~λ/1000) - far beyond the light diffraction limit (~λ/2) - ensuring optical imaging and spectroscopic identification without integrating the information

from mixed phases [17,22–34]. This fine resolution is especially helpful in studying phase transitions close to the critical temperature since the areal averaging in traditional far-field measurement techniques can hinder the data interpretation in systems with complex phases. s-SNOM is able to distinguish different phases in the coexistence region and directly accesses

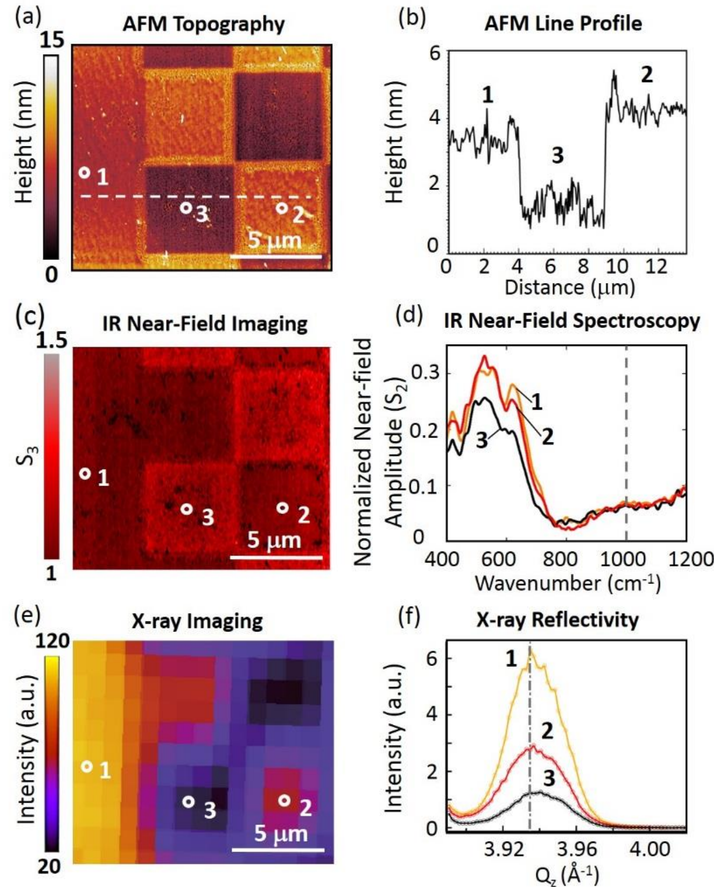

fundamental properties of the materials, enabling direct mapping of the IR electronic structure at extreme subwavelength scales [32–34]. The unique sensitivity of s-SNOM facilitates the strain engineering presented in this study.

Figure 2 | Near-field nano-spectroscopy and micro-x-ray diffraction at room temperature. (a) AFM topography at the edge of a checkerboard pattern with 5 x 5 μm boxes. Three distinct locations on the pattern are identified: ① unpatterned region, ② unetched-substrate patterned region, and ③ etched-substrate patterned region. (b) Topography profile along the white dashed line in (a). (c) Room temperature near-field image collected at ~10 μm showing the IR response of the same pattern as in (a). (d) Broadband near-field spectra collected at each of the regions identified in (a) and (c), showing a shift in the phonon amplitude within the patterned region (curve 3). The unpatterned regions (as indicated by curve 1 and 2) show nearly identical responses. The vertical

dashed line indicates the 10 μm wavelength where the near-field image (c) was collected. (e) Room temperature μ-XRD intensity map where the diffraction intensity at the monoclinic $(022)_m$ Bragg peak position has been used to generate the contrast. (f) Specular scans measured at various locations as labeled in (e).

In order to probe the local crystallographic structure variations in the VO_2 film, μ-XRD is performed using a monochromatic 11 keV x-ray beam with sub-micron resolution at the 7-ID-C beamline of the Advanced Photon Source [35]. The x-ray beam is focused down to a spot size of ~1 μm (FWHM) by a Fresnel zone plate in our experiments, which has sufficient spatial resolution to characterize the 5 x 5 μm checkerboard patterns. Scanning x-ray imaging by diffraction intensity at the film peak position and local x-ray scattering specular scans are acquired at different temperatures from 295 K to 350 K. The variation with strain of the spatial lattice constants for different phases are obtained by analyzing the XRD specular scans.

We first studied the VO_2 films on patterned $(110)_R$ TiO_2 substrates at room temperature. Three regions on the sample can be identified: ① the unpatterned single crystal VO_2, ② the substrate-unetched region of the pattern and ③ the substrate-etched region of the pattern. These three regions are clear in AFM topography, which is shown in Fig. 2 (a). The line profile in Fig. 2 (b) shows the height variation is within several nm, as the result of the substrate etching. Near-field microscopy is performed on the same area simultaneously with the AFM measurements. At room temperature, very little contrast is evident in the third harmonic near-field signal (Fig. 2 (c), S_3 measured at 10 μm), indicating the entire sample is insulating. The three regions identified in the topography are examined with broadband near-field FTIR in Fig. 2 (d) using the SINS synchrotron beamline at the ALS, Berkeley. The second harmonic (S_2) of the near-field response of a known phonon mode of VO_2 [37] is shown to decrease by ~15% in the substrate-etched region ③, indicating a variation in the local crystal orientation due to the strain-engineering. To characterize the local crystallinity, a μ-XRD intensity map of the patterned region at $(022)_M$ peak is shown in Fig. 2 (e), highlighting the change of the Bragg peak as a result of the substrate patterning. The three representative locations of the pattern are indicated in (e) and the corresponding diffraction peaks are shown in (f). Moving from the unpatterned area ① to the substrate-unetched area within the pattern ②, it is clear the diffraction intensity decreases.

Moving into the substrate-etched area ③, the diffraction intensity is significantly reduced. The reduction of diffraction intensity is not due to polycrystallization as the VO_2 powder diffraction ring was not observed on the x-ray area detector (PILATUS 100K). Instead, the reduced diffraction intensity suggests that the crystal orientation of the majority VO_2 film on the etched TiO_2 substrate is not aligned along $(110)_{M.}$ Although these regions of the VO_2 film are not aligned, their orientations are not randomized either, due to the lack of a powder diffraction ring. The results shown in Fig. 2 indicate that the modified interface alters the local epitaxy of the VO_2 film, producing regions of single crystal VO_2 (unpatterned), less-aligned VO_2 (substrate-unetched region within the pattern), minimally-aligned VO_2 (substrate-etched pattern), and the intermediate areas at the border between the different regions. In addition, we find two monoclinic $(022)_M$ Bragg peaks - M and M' at room temperature can be resolved with a double Gaussian fitting (see the Supplemental Materials Fig. S3). The M peak is close to the bulk value of monoclinic VO_2 $(022)_M$ peak while the M' peak has a smaller out-of-plane lattice constant due to epitaxial strain. The peak width of the M phase gradually increased from region ① to ③ suggesting the coherence length (as measured by the inverse of the Bragg peak width and defined as the length over which crystalline order is maintained) of the M phase along the out-of-plane direction gradually decreases from region ① to ③. This reduction of the coherence length of the M phase with patterning is consistent with a relaxed (unstrained) VO_2 film, while the strained VO_2 film component M' shows no discernable coherence length differences in these three regions (see the Supplemental Materials for details).

Near-Field and μ-XRD Characterization at Elevated Temperatures. The temperature-dependent s-SNOM characterization of the infrared properties of the VO_2/TiO_2 patterns, crucial for future applications of the proposed substrate engineering technique, is presented in Fig. 3 where the insulating conductivity is in red and the metallic conductivity is in cyan. The near-field images at 11 μm demonstrate that the VO_2 on the etched regions of the TiO_2 substrate (region ③) undergo the IMT at lower temperatures than the unpatterned, highly oriented region of the film (region ①). Region ③ also lacks the characteristic anisotropic metallic stripes (cyan color) evident in the region ①. This is due to the fact that the film on the unpatterned TiO_2 surface is

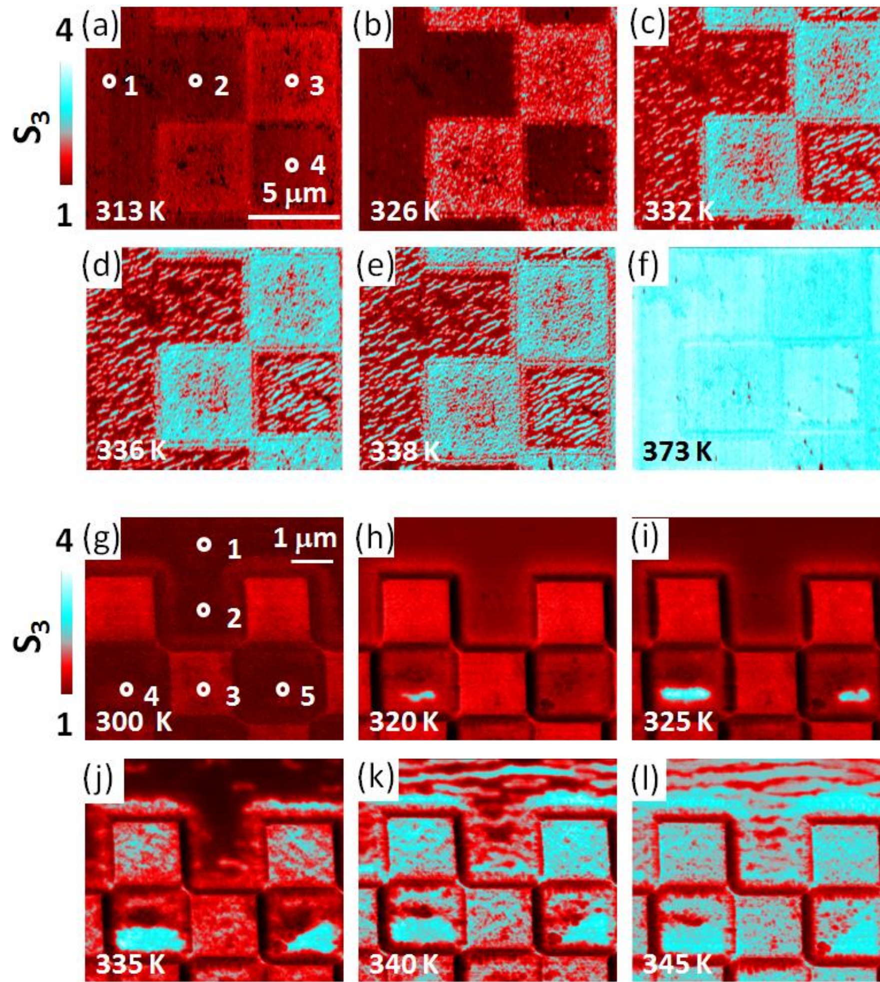

subject to a highly oriented epitaxial growth, yielding a typical stripe-like insulator to metal phase transition as observed in strained single crystalline thin films [10,11,37], while the region of the film grown on the etched substrate region is less oriented and experiences strain relief. At the highest temperatures (above 360 K) the entire sample becomes metallic, indicating the quality of the VO_2 film and the

Figure 3 │ Temperature-dependent infrared near-field images of patterned VO_2/TiO_2 at 11 μm, revealing area-dependent insulator to metal phase transitions. The metallic phase is shown in cyan and the insulating phase is in red. (a)-(f), 5 x 5 μm checkerboard patterns at (a) 313 K, (b) 326 K, (c) 332 K, (d) 336 K, (e) 338 K, (f) 373 K. (g)-(l), 1.5 x 1.5 μm checkerboard patterns on the same sample, at (g) 300 K, (h) 320 K, (i) 325 K, (j) 335 K, (k) 345 K, (l) 350 K.

robustness of the phase transition even with the etched TiO_2 substrate. By measuring checkerboard patterns with different lateral sizes and orientations fabricated on the same film, we have reached the following conclusions:

regions ①, ②, and ④ (as shown in Figure 3) exhibit striped phase coexistence, while region ③

supports localized nucleation of the metallic state; region ① has a higher transition temperature than region ③ and ④; all regions complete the IMT above 350 K and the signal levels are close to each other at the fully metallic state; and the in-plane orientation of the checkerboard does not play a major role in the mesoscopic phase separation.

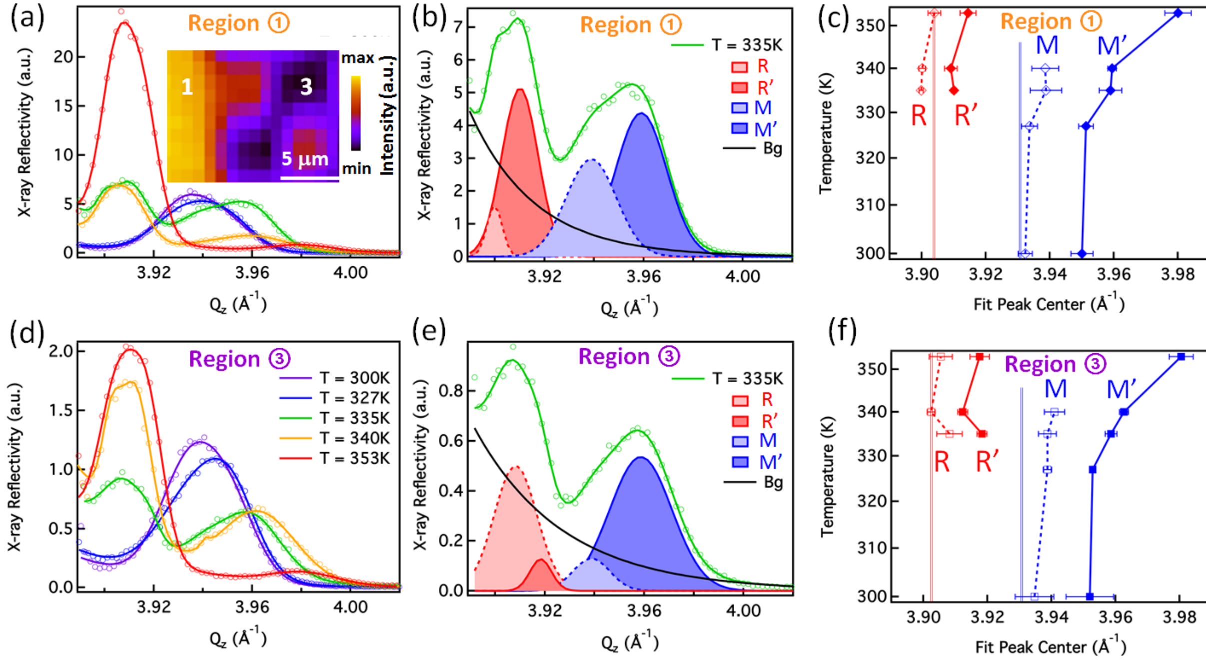

Figure 4 │ μ-XRD analysis of the VO_2/TiO_2 patterned area. Micro-XRD intensity map taken at the film peak position at 300 K is shown in the inset of (a). The measurements in region ① are summarized in (a) the specular x-ray diffraction scans at various temperatures corresponding to the legend in (d), (b) the representative fitting of diffraction peaks at T=335 K, and (c) the extracted temperature-dependent Bragg peak positions. (d-f) Show the corresponding plots for region ③.

The corresponding temperature dependent structural variation across the same checkerboard pattern in Fig. 3 (a) is presented in Fig.4. The x-ray reflectivity data and fit, the fraction of the component phases, and the peak locations of the component phases as a function of temperature are plotted for region ① (Fig. 4 (a)-(c)) and region ③ (Fig. 4 (d)-(f)). The x-ray intensity map taken at the VO_2 $(022)_M$ film peak position at 300 K is shown in the inset of Fig. 4 (a). Fig. 4(a) and (d) show the specular scans measured in the vicinity of the VO_2 $(022)_M$ peak and $(220)_R$ peak as a function of out-of-plane scattering vector, $Q_z = 4\pi\sin(2\theta/2)/\lambda$, where 2θ is the scattering

angle and λ is the wavelength at different temperatures. We found that in regions ① and ③, two sets of monoclinic $(022)_M$ peaks (below ~340 K) and two sets of rutile $(220)_R$ peaks (above ~330K) can be identified. As discussed earlier, at room temperature two monoclinic $(022)_M$ peaks in the x-ray reflectivity, noted as M and M', can be clearly resolved with the fitting. The M peak is close to the bulk value of monoclinic VO_2 $(022)_M$ peak while the M' peak has a smaller out-of-plane lattice constant. Above ~340 K, two rutile $(220)_R$ peaks R and R' can be identified. The R peak is close to the bulk value while R' has a smaller out-of-plane lattice constant. At 335 K, in the vicinity of phase transition temperature, all four peaks (M, M', R, R') can be clearly observed, as demonstrated in Fig. 4 (b) and 4 (e). Although the absolute intensity of the x-ray reflectivity at region ③ is much lower compared to that observed at region ①, the two-peak features in both locations are similar. The bulk values are shown as vertical lines in Fig. 4 (c) and 4 (f), calculated as $d \approx 3.1978$ Å for $(011)_M$ and $d \approx 3.2201$ Å for $(110)_R$.

The main structural differences between region ① and region ③ are as follows. First, at 335 K, the R phase in region ① has an out-of-plane lattice constant slightly larger than the bulk value (Fig. 4 (c)). It leads to a smaller in-plane lattice constant than the bulk value along $[001]_R$ axis due to the Poisson effect [38], which explains the occurrence of the metallic stripes in region ① below the bulk-T_c (~340 K) [39]. In region ③, the Rutile phase has a slightly smaller lattice constant than the bulk value (Fig. 4 (f)) and the occurrence of the metallic nucleation in region ③ is mostly due to the parts of the VO_2 film with out-of-plane orientations other than $[110]_R$. The second difference between region ① and ③ is the fraction of the component phases at the same temperature. In region ③, the R' peak strengthens at a lower temperature than in region ①, while the R peak strengthens at a higher temperature than in region ① (see the Supplemental Materials Fig. S3).

Discussion

The μ-XRD measurement is consistent with the electronic phase separation and the broad hysteresis of the VO_2 films observed in the near-field images. The alternating relaxed-tensile-relaxed strain environment modulated the VO_2 film crystal structure so that the M, M', R, and R' phases coexist below and above 340 K. This is in agreement with the observation that the metallic and insulating states coexist below and above 340 K in the near-field (imaged as stripes in the highly oriented region ①). The significantly lower XRD intensity and slightly different strain levels in region ③ compared to region ① are in agreement with the expectation that the substrate-etched area has a multi-facet crystal domain structure, which leads to different metallic domain formation. This consistency between the near-field and μ-XRD measurements strongly suggests that the modification of the local structural phase coexistence through substrate strain engineering can lead to controlled reordering of the phase separation textures in the electronic response.

To explore the feasibility of substrate engineering with even smaller feature sizes, patterns with dimensions less than 5 μm and 1.5 μm have been fabricated (e.g. 500 nm and 1 μm). For the $(110)_R$ substrate orientation, we found that the smallest length scale at which one can still reliably distinguish the etched versus uneteched region is ~250 nm, irrespective of etch depth between 5-110 nm. This can be understood given the fact that the periodicity of the spontaneous strain-induced striped phase separation of a ~50 nm thick unpatterned $VO_2/(110)_R$ TiO_2 film is on the order of 200 nm (see the Supplemental Material in reference [11]). In other words, the periodicity of the self-organized stripes defines the ultimate 'resolution' of the substrate's impact on the local phase transitions in the films. In $VO_2/(001)_R$ TiO_2 films, this restriction no longer applies since there is no in-plane anisotropy or conductive stripe state. As a result, the 'resolution' of the pattern in $VO_2/(001)_R$ TiO_2 films is only limited by the resolution of FIB writing, which can be reliably controlled down to 50 nm.

In summary, we have demonstrated the feasibility of microscopic substrate engineering in vanadium dioxide thin films. By utilized pre-patterned substrates to control the local crystal growth and strain environment, we are able to manipulate the composite phases on a length scale close to the intrinsic self-organized phase separation in thin films. Since the epitaxial strain-

induced mesoscopic phase separation phenomenon is rather common in strongly correlated electron systems [14,40–43], this work provides a universal means for controlling the local electronic separation in phase change materials.

References

[1] J. Ge, Z.-L. Liu, C. Liu, C. Gao, D. Qian, Q. Xue, Y. Liu, and J.-F. Jia, Nat. Mater. **14**, 285 (2014).

[2] M. Li, T. Graf, T. D. Schladt, X. Jiang, and S. S. P. Parkin, Phys. Rev. Lett. **109**, 196803 (2012).

[3] A. D. Caviglia, S. Gariglio, N. Reyren, D. Jaccard, T. Schneider, M. Gabay, S. Thiel, G. Hammerl, J. Mannhart, and J.-M. Triscone, Nature **456**, 624 (2008).

[4] M. D. Goldflam, T. Driscoll, D. Barnas, O. Khatib, M. Royal, N. M. Jokerst, D. R. Smith, B.-J. Kim, G. Seo, H.-T. Kim, and D. N. Basov, Appl. Phys. Lett. **102**, 224103 (2013).

[5] M. D. Goldflam, M. K. Liu, B. C. Chapler, H. T. Stinson, A. J. Sternbach, a. S. McLeod, J. D. Zhang, K. Geng, M. Royal, B. J. Kim, R. D. Averitt, N. M. Jokerst, D. R. Smith, H. T. Kim, and D. N. Basov, Appl. Phys. Lett. **105**, (2014).

[6] J. Rensberg, S. Zhang, Y. Zhou, A. S. McLeod, C. Schwarz, M. Goldflam, M. Liu, J. Kerbusch, R. Nawrodt, S. Ramanathan, D. N. Basov, F. Capasso, C. Ronning, and M. A. Kats, Nano Lett. **16**, 1050 (2016).

[7] M. K. Liu, B. Pardo, J. Zhang, M. M. Qazilbash, S. J. Yun, Z. Fei, J. H. Shin, H. T. Kim, D. N. Basov, and R. D. Averitt, Phys. Rev. Lett. **107**, 66403 (2011).

[8] M. Liu, H. Y. Hwang, H. Tao, A. C. Strikwerda, K. Fan, G. R. Keiser, A. J. Sternbach, K. G. West, S. Kittiwatanakul, J. Lu, S. A. Wolf, F. G. Omenetto, X. Zhang, K. A. Nelson, and R. D. Averitt, Nature **487**, 345 (2012).

[9] J. Zhang, X. Tan, M. Liu, S. W. Teitelbaum, K. W. Post, F. Jin, K. A. Nelson, D. N. Basov, W. Wu, and R. D. Averitt, Nat. Mater. **15**, 956 (2015).

[10] M. Liu, A. J. Sternbach, M. Wagner, T. V Slusar, T. Kong, S. L. Bud, S. Kittiwatanakul, M. M. Qazilbash, A. Mcleod, Z. Fei, E. Abreu, J. Zhang, M. Goldflam, S. Dai, G. Ni, J. Lu, H. A. Bechtel, M. C. Martin, M. B. Raschke, R. D. Averitt, S. A. Wolf, H. Kim, P. C. Canfield, and D. N. Basov, Phys. Rev. B Condens. Matter Mater. Phys. **91**, 245155 (2015).

[11] M. K. Liu, M. Wagner, E. Abreu, S. Kittiwatanakul, A. McLeod, Z. Fei, M. Goldflam, S. Dai, M. M. Fogler, J. Lu, S. A. Wolf, R. D. Averitt, and D. N. Basov, Phys. Rev. Lett. **111**, 096602 (2013).

[12] J. Laverock, S. Kittiwatanakul, A. A. Zakharov, Y. R. Niu, B. Chen, S. A. Wolf, J. W. Lu,

and K. E. Smith, Phys. Rev. Lett. **113**, 216402 (2014).

[13] M. Liu, A. J. Sternbach, and D. N. Basov, Reports Prog. Phys. **80**, 014501 (2017).

[14] K. Lai, M. Nakamura, W. Kundhikanjana, M. Kawasaki, Y. Tokura, M. A. Kelly, and Z.-X. Shen, Science **329**, 190 (2010).

[15] M. Liu, M. Wagner, J. Zhang, A. McLeod, S. Kittiwatanakul, Z. Fei, E. Abreu, M. Goldflam, A. J. Sternbach, S. Dai, K. G. West, J. Lu, S. A. Wolf, R. D. Averitt, and D. N. Basov, Appl. Phys. Lett. **104**, 121905 (2014).

[16] T. Yajima, Y. Ninomiya, T. Nishimura, and A. Toriumi, Phys. Rev. B **91**, 205102 (2015).

[17] M. M. Qazilbash, M. Brehm, B.-G. B.-G. Chae, P.-C. P.-C. Ho, G. O. Andreev, B.-J. B.-J. Kim, S. J. Yun, A. V. Balatsky, M. B. Maple, F. Keilmann, H.-T. H.-T. Kim, and D. N. Basov, Science **318**, 1750 (2007).

[18] M. M. Qazilbash, M. Brehm, G. O. Andreev, A. Frenzel, P. C. Ho, B.-G. Chae, B.-J. Kim, S. J. Yun, H.-T. Kim, A. V Balatsky, O. G. Shpyrko, M. B. Maple, F. Keilmann, and D. N. Basov, Phys. Rev. B **79**, 075107 (2009).

[19] Y. Greenzweig, Y. Drezner, S. Tan, R. H. Livengood, and A. Raveh, Microelectron. Eng. **155**, 19 (2016).

[20] S. Kittiwatanakul, J. Laverock, D. Newby Jr., K. E. Smith, S. A. Wolf, J.Lu, J. Appl. Phys. **114**, 053703 (2013).

[21] K. G. West, J.Lu, J.Yu, D. Kirkwood,W. Chen, Y. Pei, J. Claassen, S. A. Wolf, J. Vac. Sci. Technol., A. **26,** 133 (2008).

[22] D. Bonnell, D. Basov, M. Bode, U. Diebold, S. Kalinin, V. Madhavan, L. Novotny, M. Salmeron, U. Schwarz, and P. Weiss, Rev. Mod. Phys. **84**, 1343 (2012).

[23] J. M. Atkin, S. Berweger, A. C. Jones, and M. B. Raschke, Adv. Phys. **61**, 745 (2012).

[24] D. A. Powell, M. Lapine, M. V. Gorkunov, I. V. Shadrivov, and Y. S. Kivshar, Phys. Rev. B - Condens. Matter Mater. Phys. **82**, 155128 (2010).

[25] B. Knoll and F. Keilmann, Nature **399**, 134 (1999).

[26] F. Keilmann, A. J. Huber, and R. Hillenbrand, J. Infrared, Millimeter, Terahertz Waves **30**, 1255 (2009).

[27] S. Amarie, T. Ganz, and F. Keilmann, Opt. Express **17**, 21794 (2009).

[28] R. M. Bakker, V. P. Drachev, H. K. Yuan, and V. M. Shalaev, Phys. B Condens. Matter **394**, 137 (2007).

[29] A. Huber, F. Keilmann, J. Wittborn, and J. Aizpurua, Nano Lett. **8**, 3766 (2008).

[30] H. A. Bechtel, E. A. Muller, R. L. Olmon, M. C. Martin, and M. B. Raschke, Proc. Natl.

Acad. Sci. U. S. A. **111**, 7191 (2014).

[31] J. Pendry, Opt. Photonics News **15**, 32 (2004).

[32] M. Schnell, A. García-Etxarri, a. J. Huber, K. Crozier, J. Aizpurua, and R. Hillenbrand, Nat. Photonics **3**, 287 (2009).

[33] M. Schnell, a. Garcia-Etxarri, J. Alkorta, J. Aizpurua, and R. Hillenbrand, Nano Lett. **10**, 3524 (2010).

[34] N. Kumar, A. C. Strikwerda, K. Fan, X. Zhang, R. D. Averitt, P. C. M. Planken, and A. J. L. Adam, Opt. Express **20**, 11277 (2012).

[35] Y. Zhu, Z. Cai, P. Chen, Q. Zhang, M. J. Highland, I. W. Jung, D. A. Walko, E. M. Dufresne, J. Jeong, M. G. Samant, S. S. P. Parkin, J. W. Freeland, P. G. Evans, and H. Wen, Sci. Rep. **6**, 21999 (2016).

[36] T. J. Huffman, P. Xu, M. M. Qazilbash, E. J. Walter, H. Krakauer, J. Wei, D. H. Cobden, H. A. Bechtel, M. C. Martin, G. L. Carr, and D. N. Basov, Phys. Rev. B **87**, 115121 (2013).

[37] M. Liu, M. Wagner, J. Zhang, A. McLeod, S. Kittiwatanakul, Z. Fei, E. Abreu, M. Goldflam, A. J. Sternbach, S. Dai, K. G. West, J. Lu, S. a. Wolf, R. D. Averitt, and D. N. Basov, Appl. Phys. Lett. **104**, 121905 (2014).

[38] J. Pelleg. *Mechanical Properties of Materials*. Springer series Solid Mechanics and Its Applications V.190; Springer Netherlands, 2013.

[39] B. Lazarovits, K. Kim, K. Haule, and G. Kotliar, Phys. Rev. B **81**, 115117 (2010).

[40] A. S. McLeod, E. van Heumen, J. G. Ramirez, S. Wang, T. Saerbeck, S. Guenon, M. Goldflam, L. Anderegg, P. Kelly, A. Mueller, M. K. Liu, I. K. Schuller, and D. N. Basov, Nat. Phys. **13**, 80-86 (2017).

[41] E. Dagotto, T. Hotta, and A. Moreo, Phys. Rep. **344**, 1 (2001).

[42] N. D. Mathur and P. B. Littlewood, Phys. Today **56**, 25 (2003).

[43] E. Dagotto, Science **309**, 257 (2005).

Acknowledgements

The authors gratefully acknowledge the efforts of M. Raschke and his group in developing the SINS instrument at the ALS. I.C. and H. W. acknowledge the support from by U.S Department of Energy, Basic Energy Sciences, Materials Sciences and Engineering Division, under Grant No.

DE-SC0012509. The use of APS is supported by the U.S Department of Energy, Office of Science, Office of Basic Energy Sciences under Contract No. DE-AC02-06CH11357.